Oligomeric Rare-Earth-Metal Halide Clusters. Three Structures Built of $(Y_{16}Z_4)Br_{36}$ Units (Z = Ru, Ir)

Sharon J. Steinwand and John D. Corbett*

Department of Chemistry, Iowa State University, Ames, Iowa 50011

Received May 29, 1996⊗

Suitable reactions in sealed Nb tubing at 850−950 °C gave good yields of a family of oligomeric cluster phases that were characterized by single-crystal X-ray diffraction means. The basic $Y_{16}Z_4$ units (~$\bar{4}$ symmetry) can be derived from 2+2 condensation of centered $Y_6Br_{12}Z$−type clusters or as tetracapped truncated tetrahedra Y_{16} that are centered by a large tetrahedral Z_4. These are surrounded by 36 bromine atoms which bridge edges or cap faces of the $Y_{16}Z_4$ nuclei and, in part, bridge to metal atoms in other clusters. The principal bonding appears to be Y−Z and Y−Br, with weaker Y−Y ($\bar{d}$ ~ 3.70 Å) and negligible Z−Z interactions. The phase $Y_{16}Br_{20}Ru_4$ ($P4_2/nnm$, $Z = 2$; $a = 11.662(1)$ Å, $c = 16.992\ (2)$ Å) is isostructural with $Y_{16}I_{20}Ru_4$ and with the new $Sc_{16}Br_{20}Z_4$ (Z = Fe, Os). Syntheses only in the presence of Ir and ABr−YBr_3 fluxes (A = K−Cs) produce $Y_{16}Br_{24}Ir_4$ ($Fddd$, $Z = 8$; $a = 11.718(3)$ Å, $b = 22.361(7)$ Å, $c = 44.702(2)$ Å), in which the electron-richer Ir interstitials are compensated by four additional bromine atoms and altered bridging between macroclusters. Larger amounts of YBr_3 yield a third example, $Y_{20}Br_{36}Ir_4$ ($Y_{16}Br_{24}Ir_4{\cdot}4YBr_3$, $I4_1a$, $Z = 4$; $a = 12.699(1)$ Å, $c = 45.11(1)$ Å). Here infinite zigzag chains of $YBr_{6/2}$ octahedra that share *cis* edges lie between and bridge to the $Y_{16}Ir_4$ clusters. All of these phases contain 60-electron, closed-shell macroclusters. $Y_{16}Br_{20}Ru_4$ and $Y_{20}Br_{36}Ir_4$ were found to exhibit temperature-independent (Van Vleck) paramagnetism with values typical of those found for other rare-earth-metal, zirconium, niobium, and tantalum cluster halides.

Introduction

A large variety of zirconium (and hafnium) cluster halides are known that contain only isolated $Zr_6X_{12}Z$ units ($X \neq F$). When the same systems are highly reduced, the double-metal-layered phases ZrX (and HfX) are formed, but no compounds with intermediate degrees of cluster condensation are known. The contrasting compositions and structures found within analogous ternary or quaternary rare-earth-metal (R) cluster systems generally reflect the lower electron counts of these elements.[1−3] A necessary feature of clusters from metals of either type is that these contain (are usually centered by) an interstitial element Z, which may span later transition metals, main-group non-metals from the second, third or, rarely, fourth periods, hydrogen, and even diatomic C_2 groups. But the rare-earth element products are distinctive in that they afford many electron-poorer examples in which cluster condensation via shared metal edges affords not only quasi-infinite halogen-sheathed chains or networks but also novel oligomeric intermediates. Only two classes of the latter have been described. One diverse group contains dimeric $R_{10}X_{16}Z$ type units, as in $Gd_6X_{16+n}(C_2)_4$ compounds (n = 0, 1,2),[3] $CsEr_{10}I_{18}(C_2)_2$,[4] $Cs_2R_{10}I_{17}Z_2$ (R = La, Pr; Z = Co, Ni), and $La_{10}I_{15}Os_2$.[5,6] Only two examples of a tetrameric oligomer are known, the result of an imagined tetrahedral (2+2) condensation of $R_6(Z)$ type clusters into $R_{16}Z_4$ core units. The tetragonal structure reported for $Y_{16}I_{20}Ru_4$[7] has not been seen during subsequent studies of La−I, Pr−I,[5] Gd−I,[8] and Pr−Br[9] systems, while only a single example of a related cubic $Gd_{20}I_{28}Mn_4$ has appeared, this structure containing $Gd_{16}I_{20}Mn_4$ units as well as a second small tetrahedral cluster Gd_4I_8.[8] The latter has been interpreted as a cationic $Gd_4I_8^{4+}$ unit that electronically counteracts the effect of encapsulation of four electron-poorer Mn interstitials in an otherwise similar tetrameric unit, i.e., $Gd_{16}I_{20}Mn_4^{4-}$ vs $Y_{16}I_{20}Ru_4$.

Our recent explorations in Y−Br and Sc−Br systems in the presence of late transition-metal elements as potential interstitials have revealed not only several more $R_{16}X_{20}Z_4$ compounds but also other structures and compositions in which the same tetrameric cluster units serve as "building blocks". The present article describes the new $Y_{16}Br_{20}Z_4$ chemistry in some detail since only a brief communication on $Y_{16}I_{20}Ru_4$ has heretofore appeared. In addition, two remarkable structural variations of this theme are reported: for $Y_{16}Br_{24}Ir_4$, for which the number of bromide atoms available for intercluster bridging has evidently increased in direct response to the increase in the electron count of the interstitial element, and for $Y_{20}Br_{36}Ir_4$, in which unreduced YBr_3 components are intergrown in an expanded version of the second compound.

Experimental Section

Materials. The rare-earth metals utilized in the synthetic reactions were Ames Laboratory products that had been vacuum distilled. The largest impurity levels were 107−176 ppm atomic each of O and H. Scandium metal was employed in the form of strips (~3 × 5 mm) or turnings. Yttrium was cold-rolled into 2-mil sheet which was cut into small pieces (~2 × 3 mm) immediately before use. Potential interstitial

---

⊗ Abstract published in *Advance ACS Abstracts,* November 1, 1996.

(1) Corbett, J. D. In *Modern Perspectives in Inorganic Crystal Chemistry*; Parthé, E., Ed.; NATO ASI Series C; Kluwer Academic Publishers: Dordrecht, The Netherlands, 1992; p 27.

(2) Corbett, J. D. *J. Alloys Compd.* **1955**, *229*, 10.

(3) Simon, A; Mattausch, Hj.; Miller, G. J.; Bauhofer, W.; Kremer, R. K. In *Handbook on the Physics and Chemistry of Rare Earths*; Gschneidner, K. A., Eyring, L., Eds.; Elsevier-North-Holland Publishers: Amsterdam, 1991; Vol. 15, p 191.

(4) Uhrlandt, S. C.; Artelt, H. M.; Meyer, G. *Z. Anorg. Allg. Chem.* **1994**, *620*, 1532.

(5) Lulei, M.; Maggard, P. A.; Corbett, J. D. *Angew. Chem., Int. Ed. Engl.* **1996**, *33*, 1704.

(6) Lulei, M.; Martin, J. D.; Hoistad, L.; Corbett, J. D. *J. Am. Chem. Soc.*, in press.

(7) Payne, M. W.; Ebihara, M.; Corbett, J. D. *Angew. Chem., Int. Ed. Engl.* **1991**, *30*, 856.

(8) Ebihara, M.; Martin, J. D.; Corbett, J. D. *Inorg. Chem.* **1994**, *33*, 2079.

(9) Llusar, R.; Corbett, J. D. *Inorg. Chem.* **1994**, *33*, 849.

S0020-1669(96)00650-7 CCC: $12.00

elements employed were powdered Ni, Ru, Rh, Pd, Os, Ir (Johnson-Matthey, ≥99.9%), Re (Aldrich, 99.99%), Cr (AESAR, 99.5%), Fe and Cu (reagent grade), chunks of Co (AESAR, 99.5%) and Mn (Johnson-Matthey, 99.99%), and Pt strips (government issue, reagent grade).

The rare-earth-metal tribromides were prepared from the metals by the ammonium bromide route,[10] which proceeds via $(NH_4)_3RBr_6$ intermediates that are subsequently decomposed to form the RBr_3 phases which are then vacuum sublimed. Yttrium metal strips or dendrites (AESAR) were heated with a large excess of NH_4Br under Ar at 310 °C until the evolution of H_2 and NH_3 ceased (~3 d). The $(NH_4)_3YBr_6$ decomposed at 400 °C in vacuo to yield YBr_3(s), which was sublimed in a tube under dynamic vacuum at ~800 °C. $ScBr_3$ was prepared in a similar manner, with the corresponding formation, decomposition, and sublimation temperatures of 320, 550, and ~700 °C, respectively.

Syntheses. Exploratory and directed synthetic reactions were carried out on a scale of 150−200 mg within welded Nb tubes that were in turn jacketed by fused silica, as before.[7−9] Higher-purity products were gained if the interior of the loaded silica jacket was also cleaned with an $HF-H_2SO_4-HNO_3$ metal-cleaning solution and then rinsed just before it was evacuated and sealed off. All transfers took place inside a glovebox with ≤0.01 (vol) ppm of H_2O. Particular care was taken to avoid the introduction of light impurities. Oxygen, usually from H_2O, was a persistent problem that inevitably manifested itself in the formation of the pervasive ROBr and upset the loaded stoichiometries. This problem can be reduced by strong flaming of the walls of the SiO_2 jacket under high vacuum just before sealing. Even so, H_2O continues to evolve from the bulk silica[11] and even to diffuse slowly through the walls.[12] Contamination from both sources increases with time and temperature.

Products were judged both visually and with the aid of Guinier X-ray powder patterns, the yields of known phases being estimated (in terms of equivalent scattering power) on the basis of calculated patterns and their intensities. An internal standard of Si powder (NIST) added to the ground products enabled lattice constants of known phases to be refined from measured and indexed lines by least-squares means to a few parts in $\sim 10^4$.

$Y_{16}Br_{20}Ru_4$ and Analogues. The compound was first obtained from a reaction between YBr_3, Y foil, and Ru powder loaded on stoichiometry and heated at 980 °C for 24 d. This gave the new compound in 40% yield as chunks and aggregates of black intergrown crystals, plus YBr_3, YOBr (orange transparent plates), Y_5Ru_2[13] (irregular gray chunks), and another unidentified phase. Higher yields (60−85%) and better crystals were obtained from reactions loaded as Y_5Br_7Ru, Y_4Br_5Ru, and Y_3Br_3Ru, to all of which had been added ~15 mg of $AlBr_3$, which possibly aided the formation of a gaseous reduced halide that transported metal values. These systems were heated at 750 °C for 4 d, slowly ramped to 850 °C and maintained there for 4 d, ramped again (3 deg/h) to 950 °C, and held there for 2 w, followed by a slow cooling to 700 °C before turning off the furnace. (The slow heating was designed to lessen nucleation rates, but there is no ensurance that this profile is essential.) The products of particularly the bromine-richer runs included a small amount of a compound that exhibited a powder pattern nearly identical to that of $Y_{20}Br_{36}Ir_4$ (below). $Y_{16}Br_{20}Ru_4$ was obtained in nearly theoretical yield from a reaction loaded as $CsY_6Br_{10}Ru$ (slightly Ru deficient) and heated under similar conditions. Other reaction products included small amounts of YBr_3, YOBr, and, evidently, $Cs_3Y_2Br_9$ as the powder pattern contained the stronger lines calculated according to the structure of $Cs_3Y_2I_9$.[14] $Cs_3Y_2Br_9$ (a = 7.87 Å, c = 19.68 Å) was formed quantitatively in all reactions in which CsBr was present and appeared to function as a useful flux. The oligomer was also observed after quenching a reaction run at 1100 °C for 14 d, demonstrating its relatively high stability. Observed product combinations were sometimes in violation of the phase rule, indicating that equilibrium had not been reached. Identification of all reaction products was complicated by the number of phases found.

The analogous $Sc_{16}Br_{20}Z_4$ (Z = Fe, Os) were encountered during investigations of the corresponding $Sc_{20-x}Br_{28}Z_4$ phases,[15] as follows. Both occurred in more reduced (Sc−richer) systems, e.g., 20% $Sc_{16}Br_{20}Fe_4$ from compositions around Sc_3Br_3Fe, along with Sc−Fe binary phases. The composition $NaSc_4Br_4Fe$ at 840 °C for 24 d gave 60% $Sc_{16}Br_{20}Fe_4$ along with Sc and unreduced Na−Sc−Br compound(s) that evidently served as a flux, but further heating of the product for 20 d at 950 °C led to decomposition of the cluster phase. Likewise, a $Sc_3Br_2Os_2$ composition yielded ca. 50% $Sc_{16}Br_{20}Os_4$, $Sc_{11}Os_4$,[13] and small amounts of an unknown, while a similar reaction at 950 °C for 2 w, or of a $NaSc_4Br_4Os$ composition at 840 °C or 950 °C, led to two different unknowns and no $Sc_{16}Br_{20}Os_4$. The lattice parameters for Z = Fe and Os determined from 22 and 34 indexed lines in the Guinier patterns are a = 10.996(1), 11.116(1) Å and c = 16.021(4), 16.124(2) Å, respectively.

$Y_{16}Br_{24}Ir_4$. This was first observed after the composition $CsY_6Br_{11}Ir$, had been heated to 850 °C, held there 4 d, and ramped (3 deg/h) to 950 °C, where it was held for 2 w before cooling slowly. The reaction product consisted of ~50% $Y_{16}Br_{24}Ir_4$ as agglomerates of brittle black crystals grown in and around a mixture of YBr_3 (~10%), YOBr (~15%), and $Cs_3Y_2Br_9$ (~25%). A similar composition heated even more slowly (15 d) to 950 °C followed by a 2 w reaction gave the phases mentioned above plus $Y_{20}Br_{36}Ir_4$ (below) in ~20% yield. The products formed appeared to depend on not only temperature but also reaction time. The new phase was also synthesized in good yield in analogous reactions with RbI or KI at 900 °C for 5 w. These products also contained lines for $Y_6Br_{10}Ir$[9] and Y_5Ir_2 and weak lines evidencing the presence of $Rb_3Y_2Br_9$ or K_3YBr_6. (The formation of the ternary alkali-metal yttrium(III) halide phases was generally favored over cluster formation.) This oligomeric phase has been observed only in reactions that contain alkali metals and therefore $A_3Y_2Br_9$ or A_3YBr_6 as a flux, preferably with more YBr_3 to compensate for this side product. There is no evidence that any alkali metal is incorporated in the structure.

$Y_{20}Br_{36}Ir_4$. Although the powder pattern of this compound was first observed several years ago, its quantification proved to be very challenging owing to the difficulty of growing adequate single crystals. These reaction mixtures ranged from Y_3Br_2Ir and Y_2Br_2Ir compositions, which gave either ~20% each of nicely shaped black needles of $Y_6Br_{10}Ir$ and aggregates of very small black $Y_{20}Br_{36}Ir_4$ crystals or, with larger Br:Y ratios, ~40% of this phase with the balance as chunks of YIr, YIr_2, Y_5Ir_3,[13] YOBr, and even small amounts of YBr_3. Reaction mixtures in the range Y_3Br_3Ir to $Y_6Br_{10}Ir$ plus ~15 mg of $AlBr_3$ in each were heated very slowly and held at 750 °C, then 850 °C, and then 900−950 °C over a total of ~24−39 d. The one loaded as $Y_6Br_{10}Ir$ gave nearly quantitative yield of that phase[9,16] while those with smaller Br:Y ratios gave moderate to high (≥80%) yields of $Y_{20}Br_{36}Ir_4$ as well as small amounts (≤25%) of an unknown phase (or phases). Crystals of the target phase were still very small or poorly shaped. Further heating of the products of a Y_5Br_8Ir reaction at 975 °C for 36 d followed by quenching gave instead ~40% of an unidentified phase. Temperature gradients or alkali-metal halide fluxes did not aid crystal formation, the latter producing instead ternary alkali-metal yttrium(III) bromides and $Y_{16}Br_{24}Ir_4$. The best crystals came from a $Y_{10}Br_{13}Ir_3$ composition heated at 975 °C for 36 d which gave ca. 50% of the desired phase.

Structural Studies. $Y_{16}Br_{20}Ru_4$. Initial screening of crystals was done with the aid of oscillation and Laue photographs. A blocklike black chunk from a stoichiometric reaction was used for data collection at room temperature on a Rigaku AFC6R diffractometer equipped with Mo Kα radiation. Twenty reflections from a random search indexed to a primitive tetragonal cell, and Laue class 4/*mmm* was suggested by the diffractometer software and confirmed by axial photos. A hemisphere of data ($h,\pm k,\pm l$) was collected for $1° < 2\theta < 50°$, followed by measurement of three ψ scans which indicated a relatively large

---

(10) Meyer, G.; Dötsch, S.; Staffel, T. *J. Less-Common Met.* **1987**, *127*, 155.

(11) Holland, L. *The Properties of Glass Surfaces*; Chapman and Hall: London, 1966; Chapter 4.

(12) Schaeffer, H. A. In *Concise Encyclopedia of Semiconducting Materials and Related Technologies;* Mahajan, S., Kimerling, L. C., Eds.; Pergamon Press: Tarrytown, NY., 1992; p 457.

(13) Villars, P.; Calvert. L. D. *Pearson's Handbook of Crystallographic Data for Intermetallic Phases*, 2nd ed.; American Society for Metals International: Metals Park, OH, 1991; Vols. 3 and 4.

(14) Guthrie, D. H.; Meyer, G.; Corbett, J. D. *Inorg. Chem.* **1981**, *20*, 1192.

(15) Steinwand, S. J.; Corbett, J. D. Unpublished research.

(16) Payne, M. W.; Corbett, J. D. *Inorg.Chem.* **1990**, *29*, 2246.

Table 1. Selected Crystal Data and Refinement Parameters for $Y_{16}Br_{20}Ru_4$, $Y_{20}Br_{24}Ir_4$, and $Y_{20}Br_{36}Ir_4$

emp formula	Y_4Br_5Ru	Y_4Br_6Ir	Y_5Br_9Ir
fw	865.21	1027.27	1355.88
space group, Z	$P4_2/nnm$ (No. 134), 8	$Fddd$ (No. 70), 32	$I4_1a$ (No. 88), 16
lattice params			
a (Å)^a	11.662(1)	11.718(3)	12.6986(9)
b (Å)		22.361(7)	
c (Å)	16.997(2)	44.702(2)	45.11(1)
V (Å^3)	2311.6(6)	11 713(11)	7274(3)
d_{calc} (g/cm^3)	4.92	4.66	4.95
μ(Mo Kα) (cm^{-1})	383.2	409.95	427.11
R, $R_w{}^b$	0.032, 0.032	0.057, 0.055	0.043, 0.050

[a] Cell constants from 23, 27, and 26 lines in the Guinier patterns, respectively; 22 °C, $\lambda = 1.540\ 56$ Å. [b] $R = \Sigma||F_o| - |F_c||/\Sigma|F_o|$; $R_w = [\Sigma w(|F_o| - |F_c|)^2/\Sigma w(F_o)^2]^{1/2}$; $w = \sigma_F{}^{-2}$.

Table 2. Positional and Isotropic-Equivalent Thermal Parameters for $Y_{16}Br_{20}Ru_4$ ($P4_2/nnm$)^a

atom	Wyckoff posn	x	y	z	$B_{eq}{}^b$ (Å^2)
Ru	8m	0.1481(1)	$-x$	0.31976(7)	0.87(3)
Y1	8m	0.1369(1)	$-x$	0.47892(8)	1.13(4)
Y2	8m	0.1167(1)	$-x$	0.15603(9)	1.03(4)
Y3	16n	0.1329(1)	0.0815(1)	0.32681(7)	1.00(5)
Br1	16n	0.1245(1)	0.3481(1)	0.33899(6)	1.28(6)
Br2	8m	−0.1124(1)	$-x$	0.3395(1)	1.48(5)
Br3	8m	−0.1222(1)	$-x$	0.0212(1)	1.53(4)
Br4	8l	0.1196(1)	x	$^1/_2$	1.24(4)

[a] Origin at $2/m$. [b] $B_{eq} = (8\pi^2/3)\Sigma_i\Sigma_j U_{ij}a_i{}^*a_j{}^*\vec{a}_i\vec{a}_j$.

Table 3. Positional and Isotropic-Equivalent Thermal Parameters for $Y_{16}Br_{24}Ir_4$ ($Fddd$)

atom^a	x	y	z	B_{eq} (Å^2)
Ir	0.0238(2)	0.0728(1)	0.09899(5)	1.40(7)
Y1	0.0073(4)	0.0677(3)	0.0372(1)	2.1(2)
Y2	0.0086(4)	−0.0536(2)	0.8389(1)	1.8(2)
Y3	0.0423(4)	−0.0656(2)	0.3444(1)	1.8(2)
Y4	0.0092(4)	−0.0497(2)	0.0952(1)	1.6(2)
Br1	0.0032(4)	−0.0809(2)	0.1579(1)	2.1(2)
Br2	0.0028(4)	0.0592(2)	0.2273(1)	2.0(2)
Br3	0.0245(4)	0.0581(2)	0.5930(1)	2.1(2)
Br4	0.0156(5)	0.0635(3)	0.3433(2)	2.6(3)
Br5	0.0071(5)	−0.0613(2)	0.0307(2)	2.4(3)
Br6	0.0177(5)	−0.0694(3)	0.2823(2)	2.8(2)

[a] All type 32h positions; origin at $\bar{1}$.

transmission coefficient range, 0.194−1.00. Intensity statistics strongly indicated a centrosymmetric space group, and the data set exhibited systematic absences for an n-glide perpendicular to the c axis, that is $hk0$ for $h + k = 2n + 1$, while 12 reflections violated a $0kl$ ($k + l = 2n$) condition. Initial solutions were sought in $P4/nmm$ and $P4/n$. R_{av} was only slightly lower for $4/m$ than for $4/mmm$ (16.5% vs 17.1% for $I > 0$). Direct methods (SHELXS-86[17]) provided several solutions with reasonable bond lengths and coordinations, but the refinements converged at 25%. The solution in the space group $P4_2/nnm$, disregarding the noted $0kl$ violations, yielded clearly defined $Y_{16}Ru_4$ cluster units. The location of the halide atoms and the refinement were straightforward and resulted in final $R/R_w = 3.22$, 3.21%. The largest positive peak in the final difference Fourier map was 1.62 e/Å^3, located 2.27 Å from Br2, while the largest negative one was −2.09 e/Å^3. Only four reflections had final $||F_o| - |F_c||$ values greater than $5\sigma(F)$. No serious problems with absorption were suggested by the anisotropic thermal ellipsoid values; the greatest ratios of the principal axes were 1.49 for Y1 and 1.64 for Br4, both for U_{11}/U_{33}. Some data collection and refinement parameters are given in Table 1, and the positional and isotropic-equivalent thermal parameters are listed in Table 2.

The powder pattern calculated from the structure model was in excellent agreement with the observed patterns. Lattice parameters based on 23 unique lines and a tetragonal cell resulted in dimensions of $a = 11.662(1)$ Å and $c = 16.997(2)$ Å, values that were used in the distance and angle calculations.

$Y_{16}Br_{24}Ir_4$. The correct solution of this structure took some extra care and consideration. The Laue photograph of a somewhat large (0.16 × 0.20 × 0.28 mm) crystal cut from an aggregate suggested a large unit cell, and the search procedure on the Rigaku diffractometer yielded an F-centered orthorhombic cell with axes of about 11.72 Å, 22.39 Å, and 44.69 Å. Diversionary indications of a primitive cell were found to arise from tails on the strong reflections coupled with the large c axis. A quadrant of data ($\pm h,k,l$) were collected on the F-centered cell to $2\theta \leq 50°$ with a scan speed of 8° min^{-1} because of the relatively weak diffracting power of the crystal. The average of three ψ scans was employed for absorption correction. The data set after reduction exhibited not only absences appropriate to F-centering but also absences in $0kl$ ($k + l \neq 2n$), $h0l$ ($h + l \neq 2n$), $hk0$ ($h + k \neq 2n$), $h00$ ($h \neq 4n$), $0k0$ ($k \neq 4n$), and $00l$ ($l \neq 4n$). Fourteen violations of the first three in this group were ignored at this point. The intensity distribution strongly indicated the presence of a center of symmetry, and all of these conditions are unique to the space group $Fddd$.

SHELXS-86 provided a solution of all eleven atoms. Their identities were clearly defined by geometry, peak heights, distances, and bonding environments, and refinement of first positional and then isotropic thermal parameters yielded $R = 0.076$, $R_w = 0.092$. The B values were very small, negative for the Ir and one Y, until the secondary extinction coefficient was refined. Anisotropic refinement led to non-positive-definite ellipsoids for several atoms, and the ellipsoids of others were large in the $x-y$ plane. Space groups $Fdd2$ and $F222$ resulted in major correlation problems between parameters that were equivalent in $Fddd$. An alternate monoclinic cell $C2_1/c$ resulted in similar R values and did not eliminate the extreme thermal parameter problems. Weissenberg photographs of the $h0l$, $h1l$, and $h2l$ nets confirmed the cell dimensions and appropriate absences, but the first also showed a significant number of streaked spots in a net that did not correspond to the aligned crystal. These were taken to be indicative of a satellite on the data crystal. The $h1l$ and $h2l$ photographs were much cleaner and consistent with the F-centered cell.

One source of the refinement problems was thought to be systematic errors in the observed structure factors from inadequate absorption corrections, particularly if the apparent satellite was a significant fraction of the "crystal". Therefore, the ABSN93 program was applied, followed by data reduction in the CHES solution package.[18] The main advantage of the former is that it incorporates information regarding the size, shape, and absorption coefficient of the crystal in a 2θ-dependent spherical correction to the data, and this is then modified according to the ψ-scan measurements. Refinement of positional and isotropic thermal parameters with this data set yielded $R = 0.084$ and larger B values. A difference-Fourier map computed after a problem-free anisotropic refinement revealed several peaks of ≤ 3.8 e/Å^3 in a ring about the Ir atom. Application of a DIFABS[19] correction to the isotropic results as recommended yielded $R/R_w = 6.3\%/6.4\%$ and a cleaner ΔF map. Only 17 of 1182 unique reflections had $||F_o| - |F_c||$ values greater than $5\sigma(F)$. Many of these were of the $0kl$ type, and removal of two that had particularly large differences, possibly because of the satellite crystal, decreased R and R_w to 5.74% and 5.53%. The largest peak in the final difference map was 2.24 e/Å^3, 1.75 Å from Br1, and the thermal ellipsoids were very uniform except for small and reasonable anisotropic effects for bromine atoms in unique bonding situations. The powder pattern calculated from the structural model agreed very well with the observed pattern. This contains three strong lines at low angles, only about six others with $I \geq 0.1I_{max}$, and many weaker lines. Lattice parameters utilized were calculated from 27 indexed lines measured on a multiphasic Guinier pattern. The positional parameters for $Y_{16}Br_{24}Ir_4$ are listed in Table 3.

$Y_{20}Br_{36}Ir_4$. A preliminary study on the diffractometer gave a body-centered tetragonal cell, $a = 12.69$ Å, $c = 45.09$ Å, that matched data

---

(17) Sheldrick, G. M. SHELXS-86, Programs for Structure Determination. Universität Göttingen, Germany, 1986.

(18) Karcher, B. Ph.D. Dissertation, Iowa State University, Ames, IA, 1981. Jacobson, R. A. Private communication.

(19) Walker, N.; Stuart, D. *Acta Crystallogr.* **1983**, *A39*, 158.

Table 4. Positional and Isotropic-Equivalent Thermal Parameters for $Y_{20}Br_{36}Ir_4$ ($I4_1a$)[a]

atom	x	y	z	B_{eq} (Å^2)
Ir	0.1265(2)	0.2106(2)	0.15110(5)	0.6(1)
Y1	0.1411(4)	0.2057(5)	0.2118(1)	0.7(2)
Y2	0.1690(5)	0.1970(5)	0.0899(1)	0.7(3)
Y3	0.2373(5)	0.0242(5)	0.1537(1)	0.7(2)
Y4	0.1769(5)	0.2028(5)	0.3454(2)	0.7(3)
Y5	0.1518(4)	0.2004(5)	0.7171(1)	1.4(3)
Br1	0.2465(5)	0.0003(5)	0.2178(1)	1.6(3)
Br2	0.1389(6)	0.1982(6)	0.9080(1)	1.7(3)
Br3	0.1603(5)	0.1947(5)	0.2800(1)	1.7(3)
Br4	0.1548(4)	0.2023(5)	0.0231(1)	1.3(3)
Br5	0.2314(5)	0.0177(5)	0.5919(1)	1.0(3)
Br6	0.1280(6)	0.1891(6)	0.4069(1)	1.2(3)
Br7	0.1515(5)	0.1815(5)	0.6565(1)	1.7(3)
Br8	0.1569(5)	0.1939(5)	0.7784(1)	1.6(3)
Br9	0.1425(5)	0.2031(5)	0.5311(1)	1.6(3)

[a] All atoms in 16*f* positions.

calculated by TREOR[20] from 29 lines in the powder pattern. The 43 strong peaks located by the random search procedure on a better crystal consistently gave a $c/2$ cell, but axial photographs showed that the larger cell was correct. A quadrant of data ($\pm h,k,l$) were collected to $2\theta \leq 50°$ without conditions and with a reduced scan speed of 8° min^{-1}, and three ψ-scan measurements were secured and averaged. Although about 7% of all possible violations of the body-centering condition were observed, many in the $0kl$ and $h0l$ nets, these "violations" all differed by $l = 1$ from intense allowed peaks. This problem originated with streaks along c^* or overlapping scan ranges because of the large cell size. The data also exhibited systematic absences for most reflections of the type $hk0$ ($h, k \neq 2n$) and 001 ($l \neq 4n$), and intensity statistics indicated a centrosymmetric space group. The suggested space group $I4_1/a$ was later confirmed by Weissenberg photographs.

No trial models obtained from SHELXS-86 provided a reasonable solution, or in space groups $I4/m$ and $I\bar{4}$ either, but well-defined $Y_{16}Ir_4$ units were found using $I4_1$, and 20 other atoms were located with subsequent difference-Fourier calculations. However, the converged isotropic refinement at $R = 6.1\%$ showed strong correlations. The presence of additional inversion centers and a glide plane relating the positions showed that the symmetry was indeed $I4_1/a$, for which the isotropic refinement converged at $R = 5.6\%$, $R_w = 6.4\%$. Two subsequent problems with non-positive-definite ellipsoids were solved with a DIFABS absorption correction after which the isotropic and anisotropic refinements converged at $R = 4.26\%$ and $R_w = 5.02\%$, respectively. The relative sizes and shapes of the Br atom ellipsoids were consistent with their varying functionalities in the structure. The largest positive and negative peaks in the final difference Fourier calculation were 1.16 e/Å^3, 1.46 Å from Br7, and -1.49 e/Å^3. Only one reflection had $||F_o| - |F_c|| > 5\sigma(F)$.

The powder pattern calculated from the structural model was in excellent agreement with that observed, and lattice parameters were calculated from 26 indexed lines. The pattern of one reaction product in the Y−Br−Ru system also contained many strong low-angle lines characteristic of the $Y_{20}Br_{36}Ir_4$ structure type (see Syntheses), and nine strong lines from the pattern of that multiphasic sample refined to give the plausible $a = 12.701(3)$ Å, $c = 45.23(6)$ Å for $Y_{20}Br_{36}Ru_4$.

The positional and isotropic-equivalent displacement parameters for $Y_{20}Br_{36}Ir_4$ are listed in Table 4. The Supporting Information contains more details than given in Table 1 plus the anisotropic displacement parameters and angles for all three structures. These and the F_o/F_c data are also available from J.D.C.

Magnetic Susceptibilities. Powdered samples (~35 mg) were enclosed in a He-filled and sealed silica apparatus in which the sample was held between the faces of two silica rods. Data were collected on Quantum Design MPMS SQUID magnetometer from 6 to 300 K with field strength of 3 T. Diamagnetic sample holder and core corrections were applied prior to data analysis. The data were analyzed with a nonlinear least-squares-fitting program.[21]

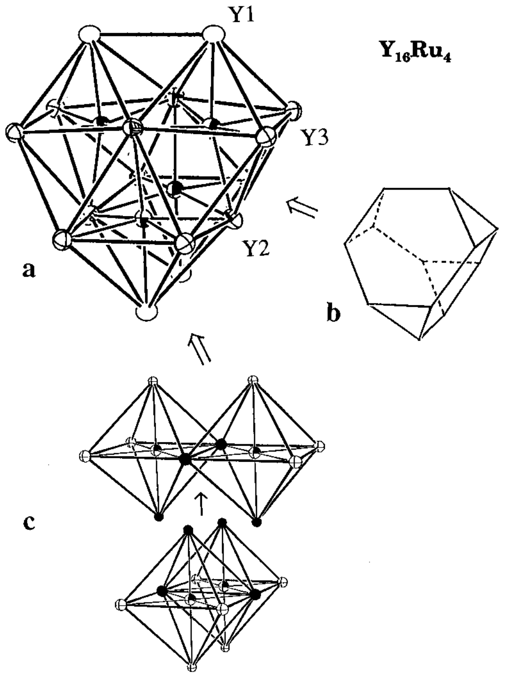

Figure 1. (a) The $Y_{16}Ru_4$ cluster ($\bar{4}2m$ symmetry) in $Y_{16}Br_{20}Ru_4$ and its derivation from (b) a truncated tetrahedron or from (c) a pairwise condensation of four Y_6Ru octahedra. $\vec{c}$ is vertical, ~[110] view. The Ru atoms are quarter-shaded and the vertices shared during condensation are black in (c).

Results and Discussion

$Y_{16}Br_{20}Ru_4$. The structure of $Y_{16}Br_{20}Ru_4$ consists of $Y_{16}Ru_4$ clusters—small bits of a hypothetical intermetallic compound—within a sphere of 36 bromine ligands that isolate each unit from, and bridge to, neighboring $Y_{16}Ru_4$ clusters. The phase is isostructural with $Y_{16}I_{20}Ru_4$, which has only been briefly described,[7] and is also found for $Sc_{16}Br_{20}Z_4$ for Z = Fe, Os (Experimental Section). The tetragonal unit cell contains two cluster units, one centered at ($^1/_4$, $^3/_4$, $^1/_4$) and the other at ($^3/_4$, $^1/_4$, $^3/_4$). The 20-atom metal cluster shown in Figure 1a consists of a 16-atom polyhedron of Y atoms centered by a relatively large tetrahedron of Ru atoms. The outer yttrium cluster can be described as a truncated tetrahedron [4 Y1 + 8 Y3] on which each of the four nearly hexagonal faces created by the truncation is further capped by a Y2 atom, i.e., a tetracapped truncated tetrahedron Y_{16}, Figure 1b. The real cluster in this case has $\bar{4}2m$ (D_{2d}) symmetry with the S_4 axis vertical. The bond distances in $Y_{16}Br_{20}Ru_4$ are listed and compared with those in $Y_{16}I_{20}Ru_4$ in Table 5; a comparable listing of angles is given in the Supporting Information.

An alternative description, emphasizing the importance of Y−Ru bonding within the structure, generates the metal cluster from four Ru-centered Y_6 octahedra via pairs of edge-sharing biclusters that are further condensed at 90° with respect to each other. This is depicted in Figure 1c. The yttrium atoms that are shared in both steps of this last route are shaded in Figure 1a and solid in Figure 1c. The Y_6Ru "octahedra" that conceptually make up $Y_{16}Br_{20}Ru_4$ (and $Y_{16}I_{20}Ru_4$) undergo substantial distortion in the process, although the Ru interstitials in both still describe tetrahedra within experimental error. Each Ru atom shifts toward the center of the polyhedron and the other

---

(20) Werner, P. E. TREOR-V5. Department of Structure Chemistry, Arrhenius Laboratory, University of Stockholm, Stockholm, Sweden, 1984.

(21) Köckerling, M. Unpublished research, Iowa State University, Ames, IA, 1993.

Table 5. Important Bond Distances (Å) in $Y_{16}Br_{20}Ru_4$ and $Y_{16}I_{20}Ru_4$[a,b]

	$Y_{16}Br_{20}Ru_4$	$Y_{16}I_{20}Ru_4$
Ru−Ru (×2)	3.357(2)	3.572(3)
Ru−Ru	3.360(3)	3.572(3)
Ru−Y1	2.712(2)	2.714(3)
Ru−Y2	2.798(2)	2.804(2)
Ru−Y2 (×2)	2.831(2)	2.837(3)
Ru−Y3 (×2)	2.686(2)	2.684(2)
$\bar{d}_{Ru-Y}$	2.757	2.760
Y1−Ru	2.712(2)	2.714(3)
Y1−Y1	3.731(5)	3.870(2)
Y1−Y2 (×2)	3.685(2)	3.769(2)
Y1−Y3 (×2)	3.629(2)	3.662(2)
$\bar{d}_{Y1-Y}$	3.672	3.746
$Y1-X2^{a-i}$	3.113(2)	3.467(3)
$Y1-X3^{i-i}$ (×2)	2.905(2)	3.097(2)
$Y1-X4^{i-i}$ (×2)	3.019(2)	3.223(2)
$\bar{d}_{Y1-X}$	2.992	3.221
Y2−Ru (×2)	2.798(2)	2.804(7)
Y2−Ru	2.831(2)	2.837(3)
Y2−Y1 (×2)	3.685(2)	3.769(2)
Y2−Y2	4.398(4)	4.284(2)
Y2−Y2 (×2)	4.458(3)	4.337(3)
Y2−Y3 (×2)	3.715(2)	3.794(2)
Y2−Y3 (×2)	3.736(2)	3.803(2)
$\bar{d}_{Y2-Y}$[c]	3.712	3.789
$Y2-X1^{i-a}$ (×2)	3.134(2)	3.309(2)
$Y2-X3^{i-i}$	3.015(2)	3.199(3)
$\bar{d}_{Y2-X}$	3.094	3.272
Y3−Ru	2.686(2)	2.684(2)
Y3−Y1	3.629(2)	3.662(2)
Y3−Y2	3.715(2)	3.794(2)
Y3−Y2	3.736(2)	3.803(2)
Y3−Y3	3.535(3)	3.581(3)
Y3−Y3	3.779(3)	3.920(3)
$\bar{d}_{Y3-Y}$	3.679	3.752
$Y3-X1^{i-a}$	2.937(2)	3.123(2)
$Y3-X1^{i-a}$	2.953(2)	3.132(2)
$Y3-X1^{a-i}$	3.118(2)	3.417(2)
$Y3-X2^{i-a}$	2.890(3)	3.115(2)
$Y3-X4^{i-i}$	2.981(1)	3.218(2)
$\bar{d}_{Y3-X}$	2.976	3.201
$X1^{i-a}-Y2$	3.134(2)	3.309(2)
$X1^{i-a}-Y3$	2.937(2)	3.123(2)
$X1^{i-a}-Y3$	2.953(2)	3.132(2)
$X1^{a-i}-Y3$	3.118(2)	3.417(2)
$X2^{a-i}-Y1$	3.113(2)	3.467(3)
$X2^{i-a}-Y3$ (×2)	2.890(3)	3.115(2)
$X3^{i-i}-Y1$ (×2)	2.905(2)	3.097(2)
$X3^{i-i}-Y2$	3.015(2)	3.199(3)
$X4^{i-i}-Y1$ (×2)	3.019(2)	3.223(2)
$X4^{i-i}-Y3$ (×2)	2.981(1)	3.218(2)
X−X	>3.71	>3.94
$\bar{d}_{Y-Y}$[c]	3.687	3.761
$\bar{d}_{Y-X}$	3.000	3.219

[a] Reference 6. [b] a and i designate outer (terminal) and inner (bridging or capping) connectivities of the halide to Y atoms. [c] Y2−Y2 distances not included.

Ru atoms, so that *trans* angles Y1−Ru−Y2 and Y2−Ru−Y3 in the bromide become 165.5 and 164.2° (×2), respectively, and the related *cis* angles are notably smaller than 90°. The Y1 atoms follow the movements of the Ru atoms, maintaining apical positions, while the Y2 atoms deviate farthest from ideal octahedral geometry. The Y2−Y2 distances that make up the shared edges of the imagined biclusters are more than 0.7 Å greater than other Y−Y distances that define each "octahedron" (>0.50 Å greater in the iodide), while a second set of slightly longer Y2−Y2 separations constitute the edges shared between bioctahedra. Neither of these longer Y2−Y2 distance types is marked in Figure 1a or considered in distance averages.

Bond distances within the clusters are comparable to those found in other reduced rare-earth-metal halide compounds. The Y−Ru distances in $Y_{16}Br_{20}Ru_4$ range from 2.686(2) to 2.831(2) Å (to Y2), with an average of 2.757 Å, substantially identical to those in the iodide cluster. These distances are well within the range of those observed in other Ru-centered Y octahedra, as in $Y_6I_{10}Ru$[22] and Y_3I_3Ru,[23] and are shorter than the sum of Pauling's single-bond metallic radii, 2.862 Å.[24] The Y−Ru interactions appear to be the fixed and strong features of the bonding. Distances between neighboring Y atoms in the bromide range from 3.535(3) to 3.779(3) Å with $\bar{d}_{Y-Y} = 3.687$ Å, which corresponds to a Pauling bond order of 0.17. The latter dimensions appear to be primarily fixed by the size of the interstitial. Each Y1 and Y3 is bonded to five other Y atoms in the cluster, while Y2 is bonded to, and nearly coplanar with, six other Y atoms, which results in a slight increase in the average Y2−Y distance. The Ru−Ru separations of 3.36 Å correspond to a Pauling bond order of 0.04 and imply that Ru−Ru bonding is negligible. Thus, Z_4 tetrahedra in some subsequent figures are outlined solely to provide geometric reference.

Three types of $R_{16}Z_4$ distortions in these compounds can be systematized as (1) the effects of cluster condensation of R_6Z in all $Y_{16}Z_4$ units, (2) the result of changes in halide size, and (3) more complex effects based on both the relative sizes of host R and interstitial Z and electronic factors. Details for the last will follow the presentation of results on new $R_{19}X_{28}Z_4$ compounds,[15] but the first two are easily perceived in $Y_{16}Br_{20}Ru_4$ and $Y_{16}I_{20}Ru_4$, which lie at one extreme in a series of eight oligomer structures. Although ideal octahedra fit together perfectly to form a tetramer, Figure 1c, this would leave the apical Y1 with only four Y neighbors, the waist Y3 with five, and the fused Y2 vertices with nine. Such a disparity in degrees of metal bonding is uncommon in rare-earth-metal halide cluster chemistry. However, the observed shift of the apical Y1 atom pairs toward each other and toward the center of the oligomer can be imagined to give an additional Y1−Y1 bond without loss, while the Ru atoms follow and move toward each other in order to maintain suitable Y−Ru distances. Short Ru−Y2 distances that would otherwise develop from this shift are avoided by motion of the Y2 atoms outward, with virtual loss of the shared equatorial Y2−Y2 bond between atoms that already have an unusually high number of Y neighbors. This fictitious scenario thus allows Y−Y interactions to be optimized without sacrificing what is probably the dominant Y−Ru bonding. Interestingly, the largest distortions observed upon substitution of Br by I are the marked (0.14 Å) increases in the relevant Y1−Y1 and Y3−Y3 distances that appear upon pairwise bicluster condensation coupled with ~0.12 Å decreases in the two types of Y2−Y2 distances, meaning the cluster "breathes" less. The transition from bromide to iodide is accompanied by 0.08 and 0.21 Å increases in average Y−Y and Ru−Ru distances. In many octahedral cluster halides, the replacement of Br (or Cl) by I causes an increase in cluster size as a result of increased matrix or steric effects[1] because of increased packing limitations (X···X repulsions) in the infinite crystalline array.

---

(22) Hughbanks, T.; Corbett. J. D. *Inorg. Chem.* **1989**, *28*, 631.

(23) Payne, M. W.; Dorhout, P. K.; Kim, S.-J.; Hughbanks, T. R.; Corbett, J. D. *Inorg. Chem.* **1992**, *31*, 1389.

(24) Pauling, L. *The Nature of the Chemical Bond*, 3rd ed.; Cornell University Press: Ithaca, NY., 1960; p 403.

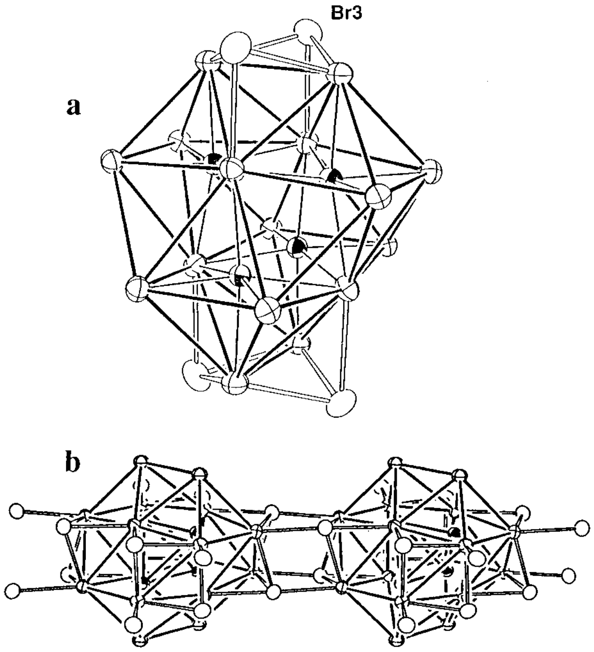

Figure 2. Two bonding modes for bromine atoms (open ellipsoids) in $Y_{16}Br_{20}Ru_4$: (a) Br3 atoms capping Y1−Y1−Y2 triangular faces and (b) Br1 atoms capping Y2−Y3−Y3 triangular faces and bonding exo to Y3 in an adjacent cluster.

On the basis of prior experience with isolated clusters,[1,2] the halides in the $Y_{16}X_{20}Ru_4$ (and other) phases would be expected to bond to free metal orbitals on the surfaces of the clusters by bridging metal edges as well as bonding exo at Y vertices in other oligomers, thus insulating these units from each other and preventing further condensation. However, these oligomers demonstrate a new halide bonding mode for clusters of the early metals, the capping of triangular Y faces by Br3 and Br1, presumably because of the reduced proportion of halogen available. A μ_3-halide bonding mode on a cluster of group 3 or 4 elements has hitherto been realized mainly in Gd_2Cl_3[1−3] and Y_4Br_4Os,[25] in which infinite chains are generated when octahedra share metal edges and square antiprismatic clusters share square faces, respectively. As shown in Figure 2a, three-bonded Br3 atoms cap four Y1−Y2−Y2 faces on each oligomer, while Br1 atoms cap eight of twelve Y2−Y3−Y3 triangular faces around the waist (those with the longer intracluster Y3−Y3 edges), Figure 2b. The Br1 atoms are also bonded exo to Y3 atoms of neighboring clusters and so are designated as Br^{i-a} and Br^{a-i} connections, noting that the "inner" functions are μ_3, not μ_2. Figure 3a illustrates how $Br4^{i-i}$ atoms (shaded) simultaneously bridge Y1−Y3 edges on two oligomers, while $Br2^{i-a}$ and the complementary $Br2^{a-i}$ atoms (crossed ellipsoids) symmetrically located about pairs of $Br4^{i-i}$ (and an inversion center) bridge Y3−Y3 edges of one oligomer while occupying the exo site at Y1 cluster apices in an adjacent oligomer.

Figure 3b shows the 36 Br atoms that surround each macrocluster, the Y−Ru and Y−Br connections being drawn heavier to emphasize the octahedral network about each Y atom and what are probably the stronger bonding interactions. The Y2 atoms, which already have 6 Y and 3 Ru neighbors, lack a direct exo bond to another bromine but rather have three neighboring μ_3-Br1 atoms (Figure 2b). The exo Y−Br bonds are longer, in accordance with general observations[1] that bonding of the interstitial atom to each metal vertex always appears to be "winning" over that to the opposing exo halogen. The same environment of 36 Br atoms about each $Y_{16}Z_4$ is found in the following two structures as well.

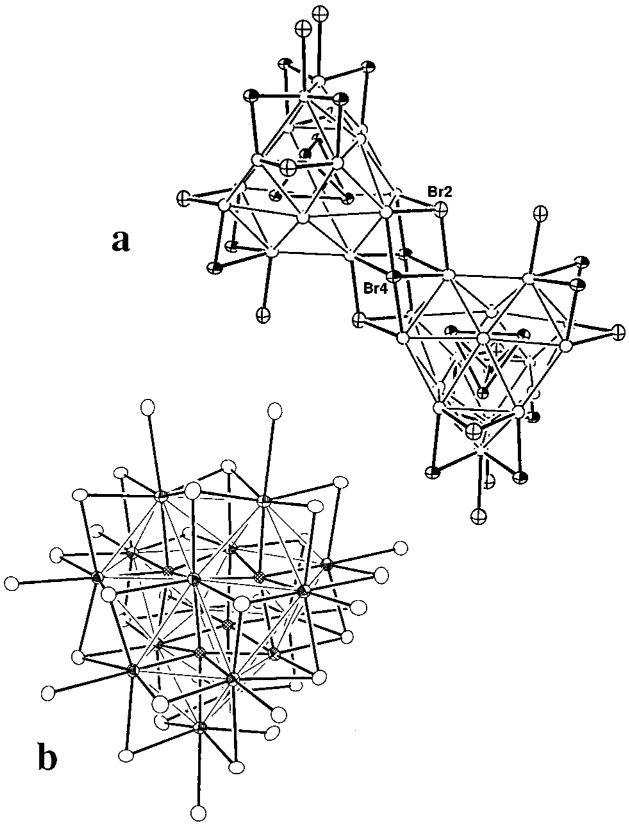

Figure 3. (a) [110] view showing the bonding modes of Br2 (crossed) as Br^{i-a} and Br4 (shaded) atoms as Br^{i-i} in $Y_{16}Br_{20}Ru_4$ (Y open, 70% ellipsoids). (b) The $Y_{16}Ru_4$ cluster with its coordination environment of 36 Br atoms, showing Br as open, Y as shaded, and Ru as cross-hatched ellipsoids. Heavy lines emphasize the strong octahedral-like bonding about each Ru.

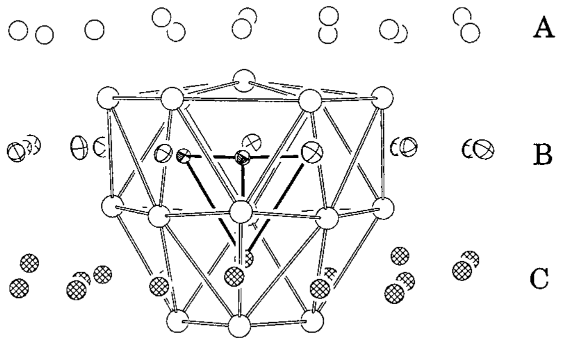

Figure 4. Cubic-close-packed description of a $Y_{16}Ru_4$ cluster and nearby bromine atoms viewed parallel to the layers.

A geometric close-packed arrangement of halide (and interstitial) atoms is a regular feature of cluster halide structural chemistry and can also be found in all three structures described herein, normal to the four pseudo-3-fold axes that pass through each Y2 and the Z_4 tetrahedron, $[2\bar{2}3]$ in the present case. Figure 4 depicts how Y atoms fill the pseudooctahedral holes between ccp Br + Ru layers that neighbor groups of Ru atoms, resulting in Y coordination by six heteroatoms (Figure 3b). The Y layers are offset slightly toward the Ru positions which themselves are shifted out of the Br layer while some Br atoms are displaced within the layers.

Overall, each oligomer is connected to eight others through two types of bromines. The $Br1^{i-a}$ and $Br1^{a-i}$ bridges pictured in Figure 5a join translationally related oligomers within the $a-b$ plane into a square network at $z = 1/4$, with a second layer

---

(25) Dorhout, P. K.; Corbett, J. D. *J. Am. Chem. Soc.* **1992**, *114*, 1697.

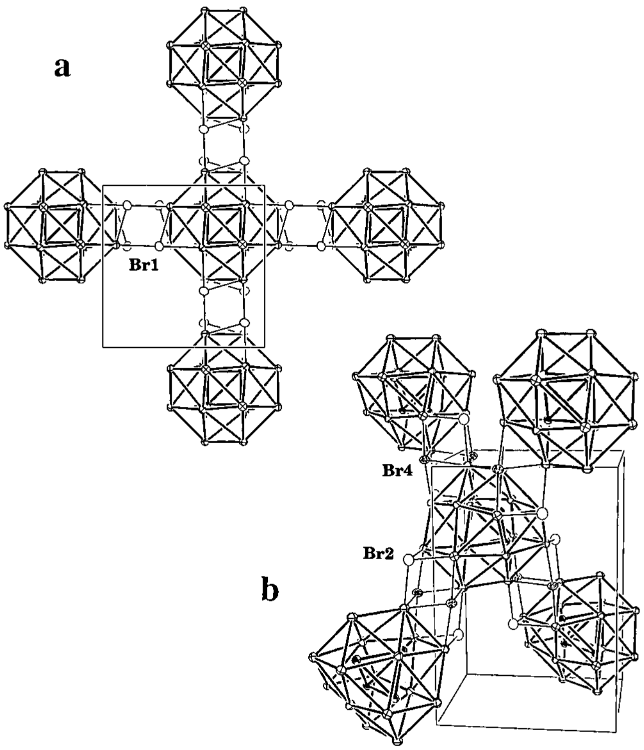

Figure 5. Intercluster bonding in $Y_{16}Br_{20}Ru_4$ (a) via Br1 atoms to form a square network within the *a*−*b* plane and (b) via $Br2^{i-a}$ and $Br4^{i-i}$ (dotted) atoms in a pseudotetrahedral arrangement of clusters along $\vec{c}$. $\vec{b}$ is horizontal in both views.

at $z = {}^{3}/_{4}$ directly above and below the holes of the first layer (at ±*a*/2, ±*b*/2) to give an ..AB.. stacking pattern. Each cluster is bridged via $Br4^{i-i}$, $Br2^{i-a}$, and $Br2^{a-i}$ to four neighbors in the adjacent layers to form a pseudotetrahedral array, as shown in Figure 5b, the clusters being rotated by 90° around $\vec{c}$ to bring the Y3−Y1−Y3 triangles face to face (Figure 3a). The shortest intercluster Y−Y distances occur in this direction between Y1 atoms, 4.57 Å. Four other clusters not connected to the central one form a second pseudotetrahedron, oriented such that Y2-centered hexagons are face to face. Accordingly, each cluster sits in an approximately cuboctahedral environment of eight near-neighbor and four more distant clusters.

$Y_{16}Br_{24}Ir_4$. Formation of a new example of a structure built of $R_{16}Z_4$ clusters is driven by a simple change: the four additional electrons derived from a change of interstitial from Ru to Ir are matched by four additional bromides so that the oligomers remain isoelectronic. The new structure maintains an environment around each cluster very similar to that in $Y_{16}Br_{20}Ru_4$, but the Br atoms are shared in a manner that accommodates four more per cluster.

The face-centered orthorhombic unit cell of $Y_{16}Br_{24}Ir_4$ (*Fddd*) shown in Figure 6 contains eight $Y_{16}Ir_4$ units. These are centered around sites of 222 (D_2) symmetry at (${}^{1}/_{8}$, ${}^{1}/_{8}$, ${}^{1}/_{8}$), (${}^{7}/_{8}$, ${}^{7}/_{8}$, ${}^{7}/_{8}$) (and other symmetry-related points) vs $\bar{4}2m$ for the macrocluster in $Y_{16}Br_{20}Ru_4$. The units are internally quite similar to those described for $Y_{16}Br_{20}Ru_4$ with only modest distortions. Each cluster now contains four crystallographically distinct Y atoms, as seen in Figure 7 with different shadings for each type. The truncated tetrahedron is formed by Y1, Y3, and Y4 atoms, while the pseudohexagonal faces are again capped by Y2 atoms. Perpendicular 2-fold axes parallel to $\vec{a}$, $\vec{b}$, and $\vec{c}$ axes bisect pairs of Y3−Y3, Y4−Y4, and Y1−Y1 edges, respectively. Distances within the structure are given in Table 6, while the corresponding angles are in the Supporting Information. The loss of mirror symmetry is evident; Y1−Y3 and Y1−Y4 bond lengths differ by 0.10(1) Å, and the two Y2−Y1 distances, by 0.06(1) Å. The three independent Ir−Ir distances range from 3.294(4) to 3.328(4) Å.

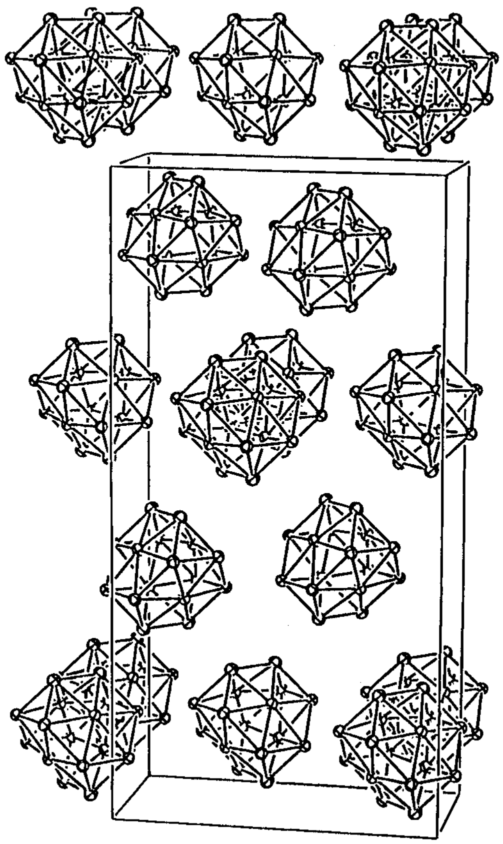

Figure 6. ∼[$\bar{1}$00] view of the unit cell of orthorhombic $Y_{16}Br_{24}Ir_4$ illustrating the face-centered nature of the cluster packing. $\vec{b}$ is horizontal; $\vec{c}$ is vertical. All Br and Ir atoms are omitted for clarity.

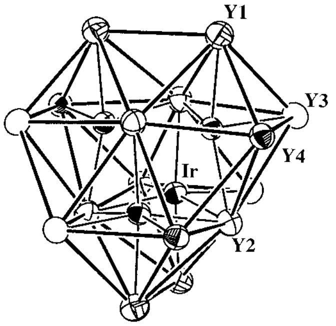

Figure 7. [110] view of a $Y_{16}Ir_4$ cluster unit in $Y_{16}Br_{24}Ir_4$ with the four types of Y atoms indicated $\vec{c}$ vertical; 222 (D_2) symmetry). Compare Figure 1a.

Most average bond distances within the $Y_{16}Ir_4$ clusters are slightly larger than those found above but still smaller than those observed in $Y_{16}I_{20}Ru_4$. The unique six-bonded Y2 atoms again have larger Y2−Y and Y2−Ir separations, and the Y2−Y2 (non-bonding) distances are nearly 0.1 Å larger in the $Y_{16}Ir_4$ cluster than in $Y_{16}Ru_4$. The average Y−Ir distance, 2.787 Å, is 0.030 Å larger than the previous average Y−Ru distance, fairly consistent with Pauling's single-bond radii,[24] which increase ∼0.02 Å from Ru to Ir; the average Ir−Ir bond order is still only 0.05. The placement of the Ir atoms is evidently dictated largely by optimization of their bonding to Y. The Y_6Ir "octahedra" that make up the oligomeric $Y_{16}Ir_4$ are more irregular than previously, with the Ir atoms displaced more toward the center of the oligomer so that the *trans* angles across each "octahedron" (Y2−Ir−Y) are 1.6−2.4° less than above. As in all oligomers, each Ir atom is distinctly closer to the metal

Table 6. Closer Atom Separations in $Y_{16}Br_{24}Ir_4$ (Å)

Ir−Ir	3.294(4)	Y2−Y1	3.757(7)	Y3−Ir	2.724(5)	Br1−Y2[a]	3.013(8)
Ir−Ir	3.322(4)	Y2−Y1	3.697(8)	Y3−Br3[a]	3.144(7)	Br1−Y4	2.890(9)
Ir−Ir	3.328(4)	Y2−Y2[b]	4.49(1)	Y3−Br3	2.932(7)	Br1−Y4	2.874(7)
Ir−Y1	2.771(7)	Y2−Y2[b]	4.47(1)	Y3−Br3	2.909(8)	Br2−Y1	2.828(8)
Ir−Y2	2.825(6)	Y2−Y2[b]	4.54(1)	Y3−Br4	2.903(9)	Br2−Y1	2.891(7)
Ir−Y2	2.821(6)	Y2−Y3	3.749(7)	Y3−Br6	2.79(1)	Br2−Y2[a]	2.966(9)
Ir−Y2	2.833(7)	Y2−Y3	3.793(8)	$\bar{d}_{\mathrm{Y3-Br}}$	2.93	Br3−Y2[a]	3.122(7)
Ir−Y3	2.724(5)	Y2−Y4	3.735(7)	Y4−Y1	3.689(8)	Br3−Y3[a]	3.144(7)
Ir−Y4	2.750(6)	Y2−Y4	3.749(8)	Y4−Y2	3.735(7)	Br3−Y3	2.932(7)
$\bar{d}_{\mathrm{Ir-Y}}$	2.787	$\bar{d}_{\mathrm{Y2-Y}}$[b]	3.747	Y4−Y2	3.749(8)	Br3−Y3	2.909(8)
Y1−Y1	3.76(1)	Y2−Ir	2.825(6)	Y4−Y3	3.620(7)	Br4−Y3	2.903(9)
Y1−Y2	3.757(7)	Y2−Ir	2.821(6)	Y4−Y4	3.81(1)	Br4−Y4	2.873(8)
Y1−Y2	3.697(8)	Y2−Ir	2.833(7)	$\bar{d}_{\mathrm{Y4-Y}}$	3.71	Br4−Y4[a]	3.075(8)
Y1−Y3	3.590(7)	Y2−Br1[a]	3.013(8)	Y4−Ir	2.750(6)	Br5−Y1	2.901(9)
Y1−Y4	3.689(8)	Y2−Br2[a]	2.966(9)	Y4−Br1	2.890(9)	Br5−Y1[a]	3.04(1)
$\bar{d}_{\mathrm{Y1-Y}}$	3.69	Y2−Br3[a]	3.122(7)	Y4−Br1	2.874(7)	Br5−Y4	2.90(1)
Y1−Ir	2.771(7)	$\bar{d}_{\mathrm{Y2-Br}}$	3.03	Y4−Br4	2.873(8)	Br6−Y1	2.817(8)
Y1−Br2	2.828(8)	Y3−Y1	3.590(7)	Y4−Br4[a]	3.075(8)	Br6−Y3	2.79(1)
Y1−Br2	2.891(7)	Y3−Y2	3.749(7)	Y4−Br5	2.90(1)	Br1−Br1	3.59(1)
Y1−Br5	2.901(9)	Y3−Y2	3.793(8)	$\bar{d}_{\mathrm{Y4-Br}}$	2.92	Br−Br	≥3.70(1)
Y1−Br5[a]	3.04(1)	Y3−Y3	3.81(1)				
Y1−Br6	2.817(8)	Y3−Y4	3.620(7)			$\bar{d}_{\mathrm{Y-Br}}$	2.937
$\bar{d}_{\mathrm{Y1-Br}}$	2.90	$\bar{d}_{\mathrm{Y3-Y}}$	3.70			$\bar{d}_{\mathrm{Y-Y}}$[b]	3.721

[a] Corresponds to a Br atom *trans* to Ru. [b] Nonbonding distances not included in averaging.

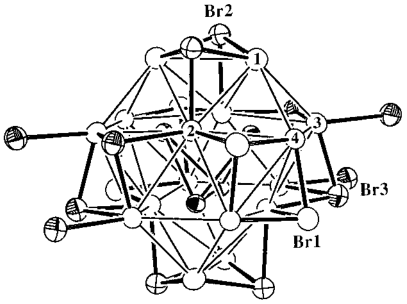

Figure 8. [110] view of three bonding modes of bromine in $Y_{16}Br_{24}Ir_4$. Br1 and Br2 cap triangular faces (Y2−Y4−Y4 and Y2−Y1−Y1, respectively) on only one cluster, while Br3 caps Y2−Y3−Y3 faces and bonds exo to Y3 in another.

atoms in the Y1−Y3−Y4 truncated faces than to the three Y2 atoms that make up the large opposed face of the surrounding “octahedron”.

Six crystallographically different Br atoms adopt four bonding modes, and their altered functionalities make up the major differences from the previous structure. As shown in Figure 8, four each of Br1, Br2, and Br3 atoms cap triangular faces, as previously; however, the Br1 and Br2 atoms are bonded to only one cluster, while Br3 atoms are simultaneously bonded exo to Y3 atoms in neighboring clusters in a manner identical to that adopted by Br1 in $Y_{16}Br_{20}Ru_4$ (Figure 2b). Figure 9 illustrates how the Br4, Br5, and Br6 atoms edge-bridge all of the triangular faces generated by truncation of the tetrahedron (Y1−Y3−Y4). The Br4 and Br5 atoms are additionally bonded exo to Y4 and Y1 atoms, respectively, in adjacent clusters, similar to the behavior of Br2 in $Y_{16}Br_{24}Ru_4$. Finally, four Br6 atoms bridge Y1−Y3 edges on only one cluster. The average Y−Br distance is 2.937 Å, 0.063 Å less than that in $Y_{16}Br_{20}Ru_4$ yet still larger than the sum of crystal radii, 2.86 Å (for six-coordinate Br^-).[26] The distance contraction is consistent with the increased number of Br atoms per cluster and the ensuing reduction in their average coordination number. The exo Y−Br distances *trans* to Y−Ru bonds are again significantly longer than others, >2.96 Å.

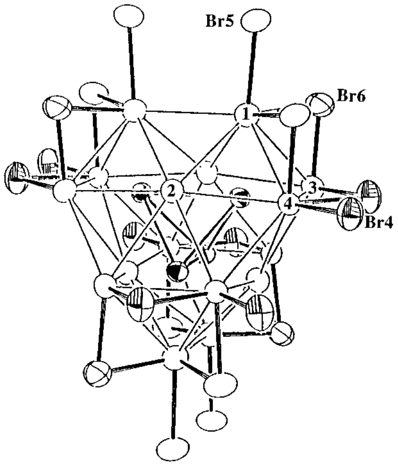

Figure 9. View of how the Br4 and Br5 atoms in $Y_{16}Br_{24}I_4$ bridge the Y3−Y4 and Y1−Y4 edges and bond exo to Y4 and Y1 in adjacent clusters, respectively, while Br6 bridges only Y1−Y3 edges of the cluster.

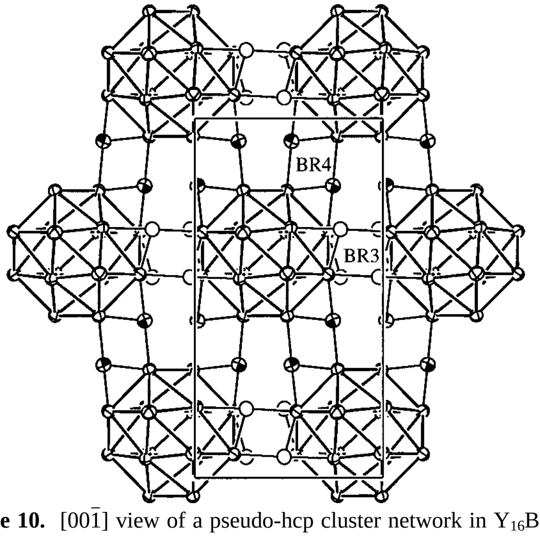

Figure 10. [00$\bar{1}$] view of a pseudo-hcp cluster network in $Y_{16}Br_{24}Ir_4$ ($z = {}^1/_8$) with interbridging by Br3 and Br4 (compare Figures 8 and 9). $\vec{a}$ is horizontal.

Every $Y_{16}Ir_4$ cluster is connected to ten neighbors via Br bridges rather than the eight previously. Six of these lie in $a-b$ planes to form a pseudo close-packed layer, Figure 10. These layers are in turn connected along $\vec{c}$ by four pair of Br5 bridges

---

(26) Shannon, R. P. *Acta Crystallogr.* **1976**, *A32, 751.*

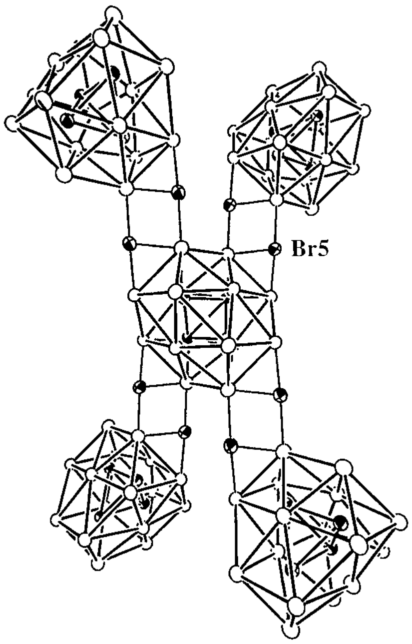

Figure 11. [$\bar{1}$00] view of intercluster bridging connections in $Y_{16}Br_{24}Ir_4$ along $\vec{c}$ (vertical) via $Br5^{i-a}$ atoms.

about each cluster, Figure 11, and these connections generate the shortest intercluster distances, 4.51 Å for Y1−Y1. This quasi-tetrahedral arrangement is similar to that in $Y_{16}Br_{20}Ru_4$, Figure 5b, but the rotation angles between cluster pairs now deviate from 90°, and the reduced and more open bridging along $\vec{c}$ results in a large expansion of the cell in that direction. The layers in Figure 10 stack along $\vec{c}$ at $z = 1/8, 3/8, 5/8, 7/8$ with the individual clusters actually related by diamond glides at $1/4, 1/4, z$, etc. As can be qualitatively perceived in Figure 6, the second cluster layer is in effect shifted by $-1/4, 1/4, 1/4$ with the clusters rotated by roughly 90° with respect to those in the first layer. The third layer is translated by $1/4, 1/4, 1/4$ from the second, with the clusters oriented as in the first layer, and so forth.

The two $Y_{16}Z_4$ examples also exhibit dimensional relationships because of related cluster packing and intercluster bridging. The strongest relationship is within the $a-b$ planes, where the cluster orientation and intercluster Br bonding modes along $\vec{a}$ and $\vec{b}$ in $Y_{16}Br_{20}Ru_4$, Figure 5a, and $\vec{a}$ in $Y_{16}Br_{24}Ir_4$, Figure 10, are identical with a common cell length of ∼11.7 Å. The pseudohexagonal (close-packed) $a-b$ plane for Ir can be obtained from the Ru network by displacement of every other (identical) row of clusters in the tetragonal $Y_{16}I_{20}Ru_4$ by $b/2$ (or $a/2$), a change that roughly doubles the repeat along $\vec{b}$ to ∼22.4 Å. This shift means the formerly interlayer-bridging Br2 atoms (Figure 3a) now bridge clusters within one layer, while the tricapping Br1 atoms (Figure 2b) no longer participate in intercluster bonding along $\vec{b}$. The c-axis length of $Y_{16}Br_{24}Ir_4$ is close to twice its b repeat because of the similarities in the bridging modes of Br5 and Br4, respectively. The relationship with c in $Y_{16}Br_{20}Ru_4$ is more complex because of the different bonding modes.

$Y_{20}Br_{36}Ir_4$. The continuation of this series to an even bromide-richer phase contains a very similar $Y_{16}Ir_4$ core, but the sharing of bromine between oligomers is further reduced by the novel incorporation of a YBr_3 component as infinite-chain units. The chains evidently contain only yttrium(III), and the compound can be expressed as $Y_{16}Br_{24}Ir_4 \cdot 4YBr_3$. The body-centered tetragonal unit cell of $Y_{20}Br_{36}Ir_4$ depicted in Figure 12 contains four oligomeric units along with the infinite zigzag chains of $Y^{III}Br^{ch}_{4/2}Br^{cl}_{2/2}$ octahedra sharing *cis* edges that run alternately along $\vec{a}$ and $\vec{b}$. The designated Br^{ch} atoms bridge

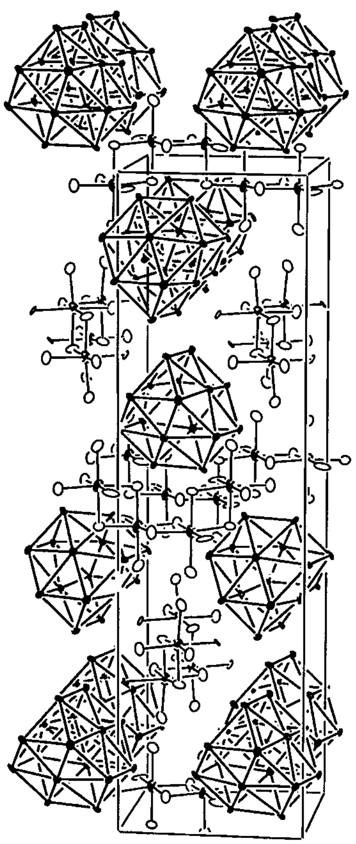

Figure 12. [$\bar{1}$00] view of the tetragonal unit cell in $Y_{20}Br_{36}Ir_4$, illustrating the body-centered nature of the cluster packing. The structure is built of $Y_{16}Ir_4$ clusters and $YBr^{ch}_{4/2}Br^{cl}_{2/2}$ chains. For clarity, only Br atoms (open ellipsoids) in the latter chains are pictured. $\vec{b}$ is horizontal; $\vec{c}$ is vertical.

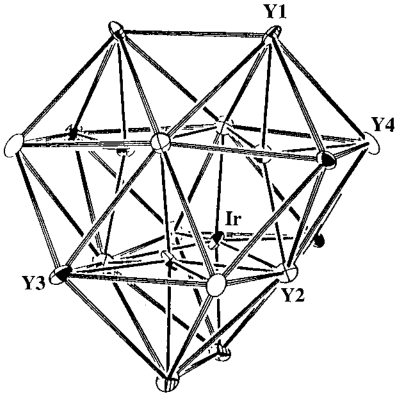

Figure 13. The $Y_{16}Ir_4$ cluster ($\bar{4}$ symmetry) in $Y_{20}Br_{36}Ir_4$ with four crystallographically distinct Y atoms indicated. $\vec{a}$ is horizontal; $\vec{c}$ is vertical.

within the chains and Br^{cl}, between chains and the $Y_{16}Ir_4$ clusters, while all other anions have been omitted from this view. The familiar $Y_{16}Ir_4$ clusters centered around $(0, 1/4, 1/8)$, $(1/2, 1/4, 3/8)$, etc. now possess $\bar{4}$ (S_4) symmetry along $\vec{c}$ and are made up of four crystallographically distinct Y atoms, as marked in Figure 13. The $\vec{b}$ axis lies nearly normal to the figure and bisects the two Y2−Y4 edges near the center.

The lack of mirror symmetry within the cluster is most pronounced in the Y1−Y3−Y4 faces generated by truncation of the imagined Y tetrahedron (Figure 1b). The Y1−Y3 distance is nearly 0.05 Å longer than Y1−Y4, Table 7, while the Y2−Y distances in the hexagonal faces are still essentially equivalent by mirror symmetry. The same is true of the Ir_4 core, where the Ir−Ir edges that parallel the Y1−Y1 edges are 0.018(4) Å longer than the rest, in line with a general but slight

Table 7. Important Bond Distances in $Y_{20}Br_{36}Ir_4$ (Å)

Ir−Ir (×2)	3.348(4)	Y2−Y3	3.767(8)	Y4−Y1	3.651(9)
Ir−Ir	3.366(5)	Y2−Y4	3.737(8)	Y4−Y2	3.737(8)
Ir−Y1	2.743(6)	Y2−Y4	3.771(9)	Y4−Y2	3.771(9)
Ir−Y2	2.817(6)	$\bar{d}_{Y2-Y}$	3.748	Y4−Y3	3.634(8)
Ir−Y2	2.836(8)	Y2−Ir	2.743(6)	Y4−Y3	3.780(7)
Ir−Y2	2.841(7)	Y2−Ir	2.817(6)	$\bar{d}_{Y4-Y}$	3.715
Ir−Y3	2.756(7)	Y2−Ir	2.836(8)	Y4−Ir	2.732(8)
Ir−Y4	2.732(8)	Y2−Br4[a]	3.022(8)	Y4−Br2[a]	3.133(9)
$\bar{d}_{Ir-Y}$	2.788	Y2−Br5[a]	3.01(1)	Y4−Br2	2.85(1)
Y1−Y1	3.75(1)	Y2−Br6[a]	2.96(1)	Y4−Br3	2.96(1)
Y1−Y2 (×2)	3.745(8)	$\bar{d}_{Y2-Br}$	3.00	Y4−Br5	2.90(1)
Y1−Y3	3.696(7)	Y3−Y1	3.696(7)	Y4−Br6	2.85(1)
Y1−Y4	3.651(9)	Y3−Y2	3.721(8)	$\bar{d}_{Y4-Br}$	2.94
$\bar{d}_{Y1-Y}$	3.714	Y3−Y2	3.767(8)	Y5−Y5[b]	4.05(1)
Y1−Ir	2.743(6)	Y3−Y4	3.634(8)	Y5−Y5[b]	4.08(1)
Y1−Br1	2.946(9)	Y3−Y4	3.780(7)	Y5−Br1	2.86(1)
Y1−Br3[a]	3.093(8)	$\bar{d}_{Y3-Y}$	3.720	Y5−Br7	2.74(1)
Y1−Br3	2.85(1)	Y3−Ir	2.756(7)	Y5−Br8	2.770(9)
Y1−Br4	2.874(8)	Y3−Br1	2.908(9)	Y5−Br8	2.78(1)
Y1−Br4	2.861(9)	Y3−Br2	2.90(1)	Y5−Br9	2.786(9)
$\bar{d}_{Y1-Br}$	2.925	Y3−Br5	2.867(9)	Y5−Br9	2.781(9)
Y2−Y1 (×2)	3.745(8)	Y3−Br6	2.91(1)	$\bar{d}_{Y5-Br}$	2.79
Y2−Y2[b] (×3)	4.50(1)	Y3−Br7[a]	2.972(9)	$\bar{d}_{Y-Y}$[b]	3.726
Y2−Y3	3.721(8)	$\bar{d}_{Y3-Br}$	2.911	Br6−Br6[c]	3.60(1)

[a] Br atom positioned *trans* to an Ir atom. [b] Longer distances not included in averaging. [c] All other Br−Br distances are ≥3.73 Å.

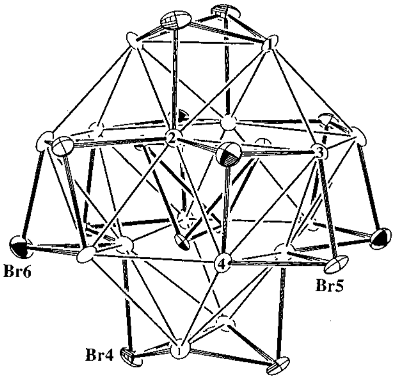

Figure 14. Bonding modes of Br4, Br5, and Br6 in $Y_{20}Br_{36}Ir_4$ which cap triangular faces (Y1−Y2−Y1, Y2−Y3−Y4, and Y2′−Y3−Y4, respectively) within the hexagon about Y2 on only one cluster. $\vec{a}$ is horizontal; $\vec{c}$ is vertical.

compression of the cluster along $\vec{c}$ that is reflected in ~0.04 Å differences in particular Y−Y distances. Despite these minor differences, the overall geometry of the clusters in $Y_{20}Br_{36}Ir_4$ is very similar to that in $Y_{16}Br_{24}Ir_4$. The average Y−Y intracluster distance of 3.726 Å (Pauling bond order = 0.15) is nearly identical to that in $Y_{16}Br_{24}Ir_4$ (3.721 Å), and the same is true for the average Y−Ir distances. The Ir−Ir distances are slightly longer (by ~0.04 Å) than previously, in parallel with the small expansion in Y−Y separations. The *trans* Y−Ir−Y angles across the imagined octahedral components are intermediate to those cited previously.

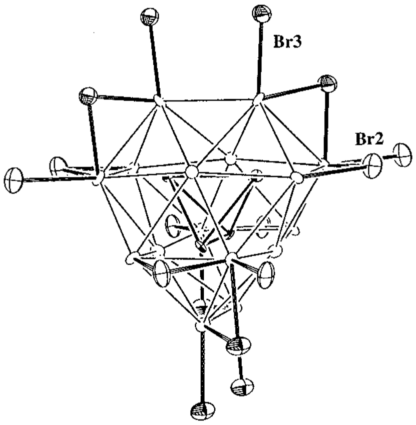

Figure 15. Bonding of Br2 and Br3 atoms in $Y_{20}Br_{36}Ir_4$ which bridge the Y3−Y4 and Y1−Y4 edges, respectively, while bonding exo to Y4 vertices in adjacent clusters (Y labels as in Figure 13).

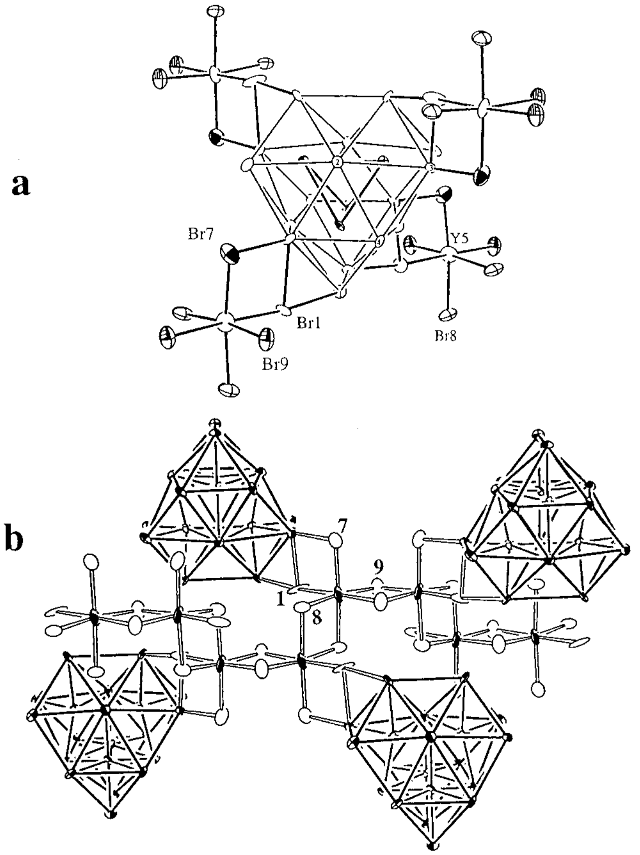

Figure 16. (a) $0\bar{1}0$ view of the bonding between the clusters and the $YBr^{ch}_{4/2}Br^{cl}_{2/2}$ chains in $Y_{20}Br_{36}Ir_4$. Br1 bridges the Y1−Y3 cluster edges while bonding to the isolated Y5, and Br7 is exo to both a Y3 vertex and the Y5 atom. Pairs of Br8 and Br9 bond exclusively within the chain, bridging *cis* edges of the Y5-centered octahedron ($\vec{a}$ is horizontal). (b) The cluster-chain interconnectivity along the zigzag $YBr^{ch}_{4/2}Br^{cl}_{2/2}$ chains. Clusters are alternately connected on both sides of and above and below the chain.

Nine types of Br atoms exhibit five basic bonding modes. Those of μ_3-Br4, -Br5, and -Br6 are defined in Figure 14, each capping four Y_3 faces on the cluster. Appropriate to the increase in bromine content, none of the eight Br5 and Br6 atoms per cluster that cap two-thirds of the Y2−Y3−Y4 faces around the waist of the cluster now bridge to another cluster, whereas half of these do in $Y_{16}Br_{24}Ir_4$ and all do in $Y_{16}Br_{20}Ru_4$. All means of direct intercluster bridging are shown in Figure 15; four Br2 atoms as Br^{i-a} bridge Y3−Y4 edges while also bonding exo to Y4 atoms in four neighboring clusters so as to form nets normal to $\vec{c}$, the same functionalities as previously (Figure 10), while $Br3^{i-a}$ atoms bridge each cluster to four others in the *c* direction ($\bar{4}$ symmetry). Figure 16a illustrates how Br1, Br7, Br8, and Br9 (keyed by shading) generate and connect the YBr_3 chains to the clusters. Four Br1 atoms that bridge Y1−Y3 edges on the clusters are also exo to the Y5 atoms that center the $YBr^{ch}_{4/2}Br^{cl}_{2/2}$ chains, while four Br7 atoms bridge Br^{a-a} between Y3 on each oligomer and Y5. The unbranched zigzag chains themselves, Figure 16b, can be viewed as Y_2Br_{10} "dimers" intrabridged by Br9 pairs and connected at both ends by pairs of Br8 bridges on *cis* edges. (A variation of this chain style occurs in $ZrCl_4$.[27]) These novel chains lie at $z \sim 0$, $^1/_4$, $^1/_2$, and $^3/_4$ between the cluster layers (below); compare Figures 12 and 16b. Four chains bridge to each oligomer, two below

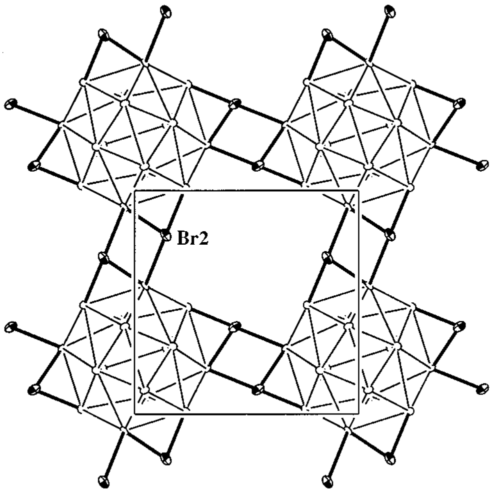

Figure 17. [00$\bar{1}$] view of the square net $Y_{16}Ir_4$ clusters in $Y_{20}Br_{36}Ir_4$ as interbridged by Br2 atoms ($z = {}^1/_8$). $\vec{a}$ is horizontal.

and two above. The Y5−Y5 distances along the chains, 4.05 Å within and 4.08 Å between dimers, are insignificant as far as bonding.

Each Y_{16} cluster is also directly bridged to eight neighboring clusters. Figure 17 depicts the square cluster network generated by Br2 bridges (Figure 15) normal to $\vec{c}$ at $z = {}^1/_8$. Other like layers at $z = {}^3/_8$, ${}^5/_8$, and ${}^7/_8$ are related by alternating *a*- and *b*-glide planes. The result in Figure 17 can also be generated from the more compact net in $Y_{16}Br_{20}Ru_4$ (Figure 5a) by a 28° clockwise rotation of the clusters and repositioning of the Br^{i-a} bridges. The direct interlayer connections by Br3 atoms along $\vec{c}$ are very similar to the interconnections by Br5 in $Y_{16}Br_{24}Ir_4$ shown in Figure 11, but they utilize different edges of the faces produced by truncation on one layer. The *c* axes of the two phases are accordingly very similar in length.

The surprising variety of structures reported here clearly arises from the number of ways in which the essential bonding needs of the oligomers can be met both internally (in electron count) and externally in filling surface bonding orbitals with different combinations of edge-bridging, face-capping, and exo-bonding bromine atoms. The change in Y:Br proportions from 4:5 through 4:6 to 5:9 in the compounds described is accompanied by progressively fewer shared or multiply-bonded bromine atoms. Thus, among the 36 bromines that cover all of these oligomeric clusters (Figure 3b), 32 are shared with/bonded to other oligomers in $Y_{16}Br_{20}Ru_4$, 24 are shared with/bonded to clusters in $Y_{16}Br_{24}Ir_4$, and only 16 are bonded to other clusters in $Y_{20}Br_{36}Ir_4$ plus 8 more that are bridged to the YBr_3 chains. The thermodynamic and kinetic interrelationships among these phases and with respect to other compounds, $Y_6Br_{10}Z$ particularly, are obviously complex too (see Synthesis—Experimental Section). One striking feature that distinguishes among the three synthetically is that $Y_{16}Br_{24}Ir_4$ was obtained only when a flux of $A_3Y_2Br_9$ or $AYBr_6$ (A = Cs−K) was used, while $Y_{20}Br_{36}Ir_4$ was never seen under these conditions because, without large composition changes, the flux formation produces an unfavorably lower YBr_3 activity.

Another dominant factor is the evident stability of these oligomers with 60 cluster-based electrons, e.g., $16 \cdot 3 - 20 + 8 \cdot 4 = 60$ in $Y_{16}Br_{20}Ru_4$. (This assignment does not require an ionic picture but requires only that Br valence levels are low-lying and filled.) The one exception, seen only once in a mixed-phase powder pattern, was apparently $Y_{20}Br_{36}Ru_4$, which would contain 56 electrons per oligomer. Isostructural oligomeric phases were not seen in comparable explorations with interstitials Cr, Mn, Re, and Pt, while Fe in a metal-richer system gave something resembling Y_2Br_2Fe ($\hat{=}Gd_2Br_2C$[28]) and Ni, possibly $Y_6Br_{10}Ni$, which is known for the iodide.[16] Some of these failures could be attributed to unfavorable electron counts, but the better explanation is that the negative results really reflect the presence of competitive phases that are more stable. The rationalization of the 60-electron needs in cluster MO terms has already appeared,[7] and more will follow along with results for $Sc_{19}Br_{28}Z_4$ phases (Z = Fe, Ru, Os) in which paramagnetic 61-electron clusters are necessary.[29]

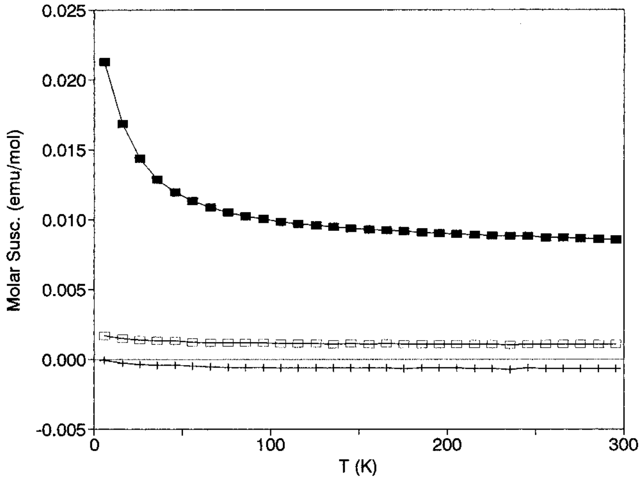

Figure 18. Molar magnetic susceptibilities as a function of temperature (K) at 3 T for $Y_{16}Br_{20}Ru_4$ (solid rectangles) and $Y_{20}Br_{36}Ir_4$ (open rectangles). The data for the latter prior to application of the diamagnetic core correction are also shown as crosses.

Support for closed-shell configurations in $Y_{16}Br_{20}Ru_4$ and $Y_{20}Br_{36}Ir_4$ has been secured in the present work through magnetic susceptibility studies that demonstrate these do not exhibit Curie−Weiss paramagnetism. Their susceptibility data as a function of temperature (6−300 K) are shown in Figure 18. The properties of both can be better described in terms of temperature-independent paramagnetism over *ca.* 50−300 K or more after the usual core corrections, with χ_{300} values of 8.54×10^{-3} and 1.06×10^{-3} emu/mol for $Y_{16}Br_{20}Ru_4$ and $Y_{20}Br_{36}Ir_4$, respectively. The value for the former appears somewhat large. This sample had been hand-selected from a mixture of ~80% of the target phase with ~5% of an unknown "Y_5Br_9Ru" and therefore may be less pure, but any impurities must behave similarly. The smaller χ_{TIP} value for $Y_{16}Br_{24}Ir_4 \cdot 4YBr_3$ comes from a selected sample that appeared from its powder pattern to contain only the fairly innocent impurities YBr_3 and $AlBr_3$. The magnitude of the data for the latter compound before correction for core diamagnetism is also shown in the figure to illustrate how small the differences are.

We are encouraged to attribute these results to Van Vleck type paramagnetism induced by the magnetic field because of numerous observations of comparable χ_{TIP} values for other cluster phases, both closed- and open-shell. The isomorphous $Y_{16}I_{20}Ru_4$ was earlier found to give $\chi_{TIP} \sim 4.9 \times 10^{-4}$ emu mol^{-1} over 60−310 K, 6% of that found here for the bromide.[7] Two different cesium salts containing isolated $Zr_6Br_{15}Be^{n-}$ clusters, one paramagnetic, yielded TIP values of (4.68−5.41)

---

(27) Hulliger, F. *Structural Chemistry of Layer-Type Phases*; D. Reidel Publishing Co.: Dordrecht, Holland, 1976; p 333.

(28) Schwanitz-Schüller, U.; Simon, A. *Z. Naturforsch.* **1985**, *B40*, 710.

(29) Steinwand, S. J.; Martin, J. D.; Corbett, J. D. To be submitted for publication.

$\times 10^{-4}$ emu (mol of clusters)$^{-1}$.[30] Recently, χ_0 terms of (6.6–9.6) $\times 10^{-4}$ emu mol^{-1} have been deduced from data for three (Curie-Weiss) paramagnetic bicluster phases, $Cs_2La_{10}I_{17}Z_2$ (Z = Ni, Os) and $La_{10}I_{15}Os_2$,[31] and 1.52 $\times 10^{-3}$ emu/mol of paramagnetic $La_{12}I_{17}Fe_2$ pertains to two isolated clusters of the $La_6I_{12}Fe$ type with considerable I^{i-i} bridging.[31] We have not found any good evidence for electron delocalization and metal-like behavior in any of these compounds. An older classic study of five paramagnetic niobium and tantalum cluster halide phases that contain $M_6X_{18}^{n-}$ units yielded similar χ_0 values of (4.8–6.5) $\times 10^{-4}$ emu mol^{-1}.[32] These were also corrected (by ~(2.2–2.7) $\times 10^{-4}$ emu mol^{-1}) for the estimated diamagnetic contributions from bonding electron pairs within the clusters (Langevin terms), which depend only on the number and size of the filled cluster MOs. Such additions would raise the results for all of the other centered clusters quoted above by about a constant amount for each cluster size. Finally, TIP behavior is also found for a number of binary cluster halides, Nb_6Cl_{14} for example.[33]

We will subsequently report on the novel, paramagnetic oligomers found in $Sc_{19}Br_{28}Z_4$ phases (Z = Fe, Ru, Os).[15] These are derived from the unique $Gd_{20}I_{28}Mn_4$ [8] (see Introduction) by systematic introduction of one disordered cation vacancy into the small clusters ($Sc_3Br_8^+$) in order to compensate for four additional electrons from the interstitials.

Acknowledgment. The authors are indebted to J. E. Ostenson for measurement of the magnetic data. This research was supported by the National Science Foundation, Solid State Chemistry, via Grants DMR-9207361 and -9510278, and was carried out in the facilities of Ames Laboratory, U.S. Department of Energy.

Supporting Information Available: Tables of crystallographic and refinement data, anisotropic displacement parameters, and intracluster bond angles for all three compounds (9 pages). Ordering information is given on any current masthead page.

IC960650X

---

(30) Qi, R.-Y.; Corbett, J. D. *Inorg. Chem.* **1995**, *34*, 1646.

(31) Lulei, M.; Martin, J. D.; Corbett, J. D. *J. Solid State Chem.* **1996**, *125*, 249.

(32) Converse, J. G.; McCarley, R. E. *Inorg. Chem.* **1970**, *9*, 1361.

(33) Simon, A.; Schnering, H.-G.; Wöhrle, H.; Schäfer, H. *Z. Anorg. Allg. Chem.* **1965**, *339*, 155.